

Decomposition-Estimation-Reconstruction: An Automatic and Accurate Neuron Extraction Paradigm (Supplementary Material)

Peixian Zhuang, *Member, IEEE*, Jiangyun Li, Qing Li, Lei Cai,
Sam Kwong, *Fellow, IEEE*, and Chongyi Li*, *Senior Member, IEEE*

Abstract—In this supplementary material, we provide 1) solution details of R-procedure, 2) proof of the solution Eq. (11) to Eq. (9), 3) proof of the solution Eq. (12) to Eq. (10), 4) proof of Eq. (15), 5) more experimental results including temporal activities extractions of dozens-of-neurons and mouse dorsal striatum, and application tests. Besides, we provide an extraction experiment on *in vivo* calcium imaging video of neurons expressing GCaMP6f in the mouse dorsal striatum including 2000 frames with sized of 128×128 in a separate file. This video results can be available at <https://github.com/zhuangpeixian/DER>.

I. METHODOLOGY

A. Solution Details of R-Procedure

Algorithm 1 summarizes respective updates to address the subproblems 1-3 for Eqs. (18)-(20) in our manuscript.

B. Proof of the Solution Eq. (11) to Eq. (9)

$$\xi(\mathbf{J}(x)) = (\mathbf{J}(x) - \mathbf{S}(x))^2 + \frac{\lambda_1}{\beta_1} \mathcal{H}(\mathbf{J}(x)) \quad (21)$$

where $\mathcal{H}(x)$ is a binary function that returns 1 if $x \neq 0$, and 0 otherwise.

Case 1.1. When $(\mathbf{S}(x))^2 \leq \frac{\lambda_1}{\beta_1}$, non-zero $\mathbf{J}(x)$ produces $\xi(\mathbf{J}(x) \neq 0) = (\mathbf{J}(x) - \mathbf{S}(x))^2 + \frac{\lambda_1}{\beta_1} \geq \frac{\lambda_1}{\beta_1} \geq (\mathbf{S}(x))^2$. Note that $\mathbf{J}(x) = 0$ leads to $\xi(\mathbf{J}(x) = 0) = (\mathbf{S}(x))^2$. Compare these two results and yield the minimum energy $\xi^*(x) = (\mathbf{S}(x))^2$ when $\mathbf{J}(x) = 0$.

Case 1.2. When $(\mathbf{S}(x))^2 > \frac{\lambda_1}{\beta_1}$ and $\mathbf{J}(x) = 0$, $\xi(\mathbf{J}(x) = 0) = (\mathbf{S}(x))^2$ still holds. But $\xi(\mathbf{J}(x) \neq 0)$ has the minimum value $\frac{\lambda_1}{\beta_1}$ when $\mathbf{J}(x) = \mathbf{S}(x)$. By comparing these two results, the minimum energy $\xi^*(x) = \frac{\lambda_1}{\beta_1}$ is produced when $\mathbf{J}(x) = \mathbf{S}(x)$.

C. Proof of the Solution Eq. (12) to Eq. (10)

$$\begin{aligned} \xi(\mathbf{G}(x)) &= (\mathbf{G}_h(x) - \nabla_h \mathbf{S}(x))^2 + (\mathbf{G}_v(x) - \nabla_v \mathbf{S}(x))^2 \\ &\quad + \frac{\lambda_2}{\beta_2} \mathcal{H}(|\mathbf{G}_h(x)| + |\mathbf{G}_v(x)|) \end{aligned} \quad (22)$$

Case 2.1. When $(\nabla_h \mathbf{S}(x))^2 + (\nabla_v \mathbf{S}(x))^2 \leq \frac{\lambda_2}{\beta_2}$, non-zero $(\mathbf{G}_h(x), \mathbf{G}_v(x))$ yields $\xi((\mathbf{G}_h(x), \mathbf{G}_v(x)) \neq (0, 0)) =$

Algorithm 1 Outline of DCNMF for Neuron Extraction

Iterate three subproblems 1-3 to convergence

Output \mathbf{P} , \mathbf{Z} and \mathbf{T} .

%% **Update spatial footprint**

$\mathbf{U} \leftarrow (\tilde{\mathbf{S}} - \mathbf{D} \cdot \mathbf{F}) \cdot \mathbf{Z}^T$

$\mathbf{V} \leftarrow \mathbf{Z} \cdot \mathbf{Z}^T$

for $k := 1$ **to** maxIter **do**

for $j := 1$ **to** K **do**

$\mathbf{p}_j \leftarrow \max(0, \mathbf{p}_j + \frac{\mathbf{u}_j - \mathbf{p}_j \cdot \mathbf{v}_j}{\mathbf{v}_{jj}})$

end for

end for

%% **Update temporal trace and spike**

$\mathbf{U} \leftarrow \mathbf{P}^T \cdot (\tilde{\mathbf{S}} - \mathbf{D} \cdot \mathbf{F})$

$\mathbf{V} \leftarrow \mathbf{P}^T \cdot \mathbf{P}$

for $k := 1$ **to** maxIter **do**

for $j := 1$ **to** K **do**

$(\mathbf{z}_j, \mathbf{t}_j) \leftarrow \text{deconvolve_and_denoise}(\mathbf{z}_j + \frac{\mathbf{u}_j - \mathbf{v}_j \cdot \mathbf{z}_j}{\mathbf{v}_{jj}})$

end for

end for

%% **Update residual errors**

$[\mathbf{U}, \Sigma, \mathbf{V}] \leftarrow \text{SVD}(\tilde{\mathbf{S}} - \mathbf{P} \cdot \mathbf{Z})$

$\mathbf{D} = \mathbf{U} \cdot \Sigma, \mathbf{F} = \mathbf{V}^T$

$(\mathbf{G}_h(x) - \nabla_h \mathbf{S}(x))^2 + (\mathbf{G}_v(x) - \nabla_v \mathbf{S}(x))^2 + \frac{\lambda_2}{\beta_2} \geq \frac{\lambda_2}{\beta_2} \geq (\nabla_h \mathbf{S}(x))^2 + (\nabla_v \mathbf{S}(x))^2$. $(\mathbf{G}_h(x), \mathbf{G}_v(x)) = (0, 0)$ leads to $\xi((\mathbf{G}_h(x), \mathbf{G}_v(x)) = (0, 0)) = (\nabla_h \mathbf{S}(x))^2 + (\nabla_v \mathbf{S}(x))^2$. By comparing these two results, the minimum energy $\xi^*(x) = (\nabla_h \mathbf{S}(x))^2 + (\nabla_v \mathbf{S}(x))^2$ is produced when $(\mathbf{G}_h(x), \mathbf{G}_v(x)) = (0, 0)$.

Case 2.2. When $(\nabla_h \mathbf{S}(x))^2 + (\nabla_v \mathbf{S}(x))^2 > \frac{\lambda_2}{\beta_2}$ and $(\mathbf{G}_h(x), \mathbf{G}_v(x)) = (0, 0)$, $\xi((\mathbf{G}_h(x), \mathbf{G}_v(x)) = (0, 0)) = (\nabla_h \mathbf{S}(x))^2 + (\nabla_v \mathbf{S}(x))^2$ still holds. However, $\xi((\mathbf{G}_h(x), \mathbf{G}_v(x)) \neq (0, 0))$ has the minimum value $\frac{\lambda_2}{\beta_2}$ when $(\mathbf{G}_h(x), \mathbf{G}_v(x)) = (\nabla_h \mathbf{S}(x), \nabla_v \mathbf{S}(x))$. Comparing these two results, the minimum energy $\xi^*(x) = \frac{\lambda_2}{\beta_2}$ is produced when $(\mathbf{G}_h(x), \mathbf{G}_v(x)) = (\nabla_h \mathbf{S}(x), \nabla_v \mathbf{S}(x))$.

*Corresponding author: Chongyi Li (lichongyi@nankai.edu.cn).

D. Proof of Eq. (15)

The dichromatic atmospheric scattering model [1] has been extensively used in image descattering, and an observed raw image \mathbf{S}_i is seen as an additive combination of the attenuation component \mathbf{B}_i^a and the airlight component \mathbf{B}_i^l : $\mathbf{S}_i = \mathbf{B}_i^a + \mathbf{B}_i^l = \mathbf{B}_i^\infty \rho e^{-\eta \mathbf{d}_i} + \mathbf{B}_i^\infty (1 - e^{-\eta \mathbf{d}_i})$, where \mathbf{B}_i^∞ is the airlight radiance, ρ and \mathbf{d}_i are the scene albedo and depth at the scene point. The attenuation coefficient η is seen as a constant, and $\mathbf{M}_i = e^{-\eta \mathbf{d}_i}$ is the depth-dependent transmission. It is typically assumed that the radiance of environmental illumination of both attenuation and airlight is approximately equal in local pixels, and $\mathbf{A}_i = \mathbf{B}_i^\infty$ denotes the environmental illumination for convenience. Thus this scattering model is refined as $\mathbf{S}_i = \mathbf{A}_i \rho \mathbf{M}_i + \mathbf{A}_i (1 - \mathbf{M}_i)$.

In the case of dark channel $\rho^{\text{dark}}(x) = 0$, we get

$$\begin{aligned} \mathbf{S}_i^{\text{dark}}(x) &= \mathbf{A}_i(x) \rho^{\text{dark}}(x) \mathbf{M}_i(x) + \mathbf{A}_i(x) (1 - \mathbf{M}_i(x)) \\ &= \mathbf{A}_i(x) (1 - \mathbf{M}_i(x)) \end{aligned} \quad (23)$$

In the case of bright channel $\rho^{\text{bright}}(x) = 1$, we get

$$\mathbf{S}_i^{\text{bright}}(x) = \mathbf{A}_i(x) \rho^{\text{bright}}(x) \mathbf{M}_i(x) + \mathbf{A}_i(x) (1 - \mathbf{M}_i(x)) = \mathbf{A}_i(x) \quad (24)$$

Afterward, the linear guided image filtering [2] is well used to filter $\mathbf{S}_i^{\text{dark}}(x)$ and $\mathbf{S}_i^{\text{bright}}(x)$ respectively, and eliminates undesirable artifacts caused by image patch-based operation. With taking the above Eqs. (23) and (24), we introduce an empirical weight coefficient ω to avoid the transmission overestimation, and deduce the final solution of the depth-dependent transmission Eq. (15) in our manuscript. Hence, the proof of Eq. (15) in our manuscript is completed.

II. MORE EXPERIMENTAL RESULTS

A. Temporal Activities Extraction of Dozens-of-Neurons

Fig. 1 exhibits temporal activities of neurons extracted by different methods, and the sparseness metric [3] (\uparrow) is adopted to evaluate their sparseness of temporal traces. As shown, the results of CNMF are severely affected by background temporal activity, and thus the lower sparseness value is produced as 0.5044. DCP-CNMF, DehazeNet-CNMF and DCNMF use different depth estimation schemes to alleviate background interference, but some residuals of background temporal activity are clear in their results, leading to low sparseness values 0.5078, 0.5057 and 0.5233, respectively. STNeuroNet employs a 3D UNet network to capture neuronal temporal dynamics and obtains relatively high sparseness 0.5613. However, Our DER separates and suppresses the complex background through L_0 -norm sparse decomposition, computes BDCP-based depth estimation to locate and enhance spatial locations of accurate neurons, and develops depth-estimation CNMF to yield better results of neuron extraction. Therefore, DER generates more accurate and sparser temporal traces of neuronal activities, and achieves the best sparseness result of 0.8144.

B. Temporal Activities Extraction of Mouse Dorsal Striatum

Fig. 2 shows temporal activities of all extracted neurons by different methods. As compared, our DER paradigm removes

complex background, estimates accurate depth, and boosts accurate neurons, thus achieving more accurate and sparser traces (0.9222) of neuronal activity than those results of CNMF (0.9075), DCP-CNMF (0.9128), DehazeNet-CNMF (0.9075), DCNMF (0.9110), and STNeuroNet (0.9210).

C. Application Test

Surgical Image Descattering. We replace the transmission estimation based on dark channel prior [8] with the proposed depth-dependent transmission model Eq. (15) in our manuscript, and then inverse the dichromatic atmospheric light scattering model [1] to obtain dehazed images. As visualized in Fig. 3, compared with two popular methods DCP [8] and DehazeNet [9] that are based on constant atmospheric light hypothesis, our method produces better descattering results, and the proposed BDCP-based depth-estimation model is used to achieve more accurate depth estimations. This test suggests the effectiveness of our depth-estimation model in descattering surgical images.

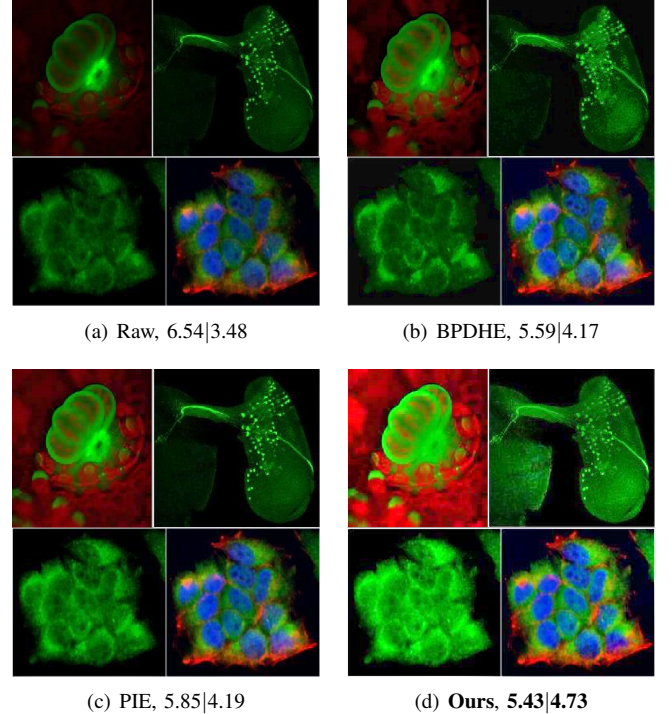


Fig. 4: **Non-uniform illumination enhancement.** NIQE [10](\downarrow) | NIQMC [11](\uparrow) are shown, and best results are marked bold. By the BDCP-based depth estimation model for estimating atmospheric light of each pixel to remove non-uniform illumination, our method outperforms BPDHE [12] and PIE [13] in better results of structure reinforcement and contrast enhancement.

Non-uniform Illumination Enhancement. Two blind metrics NIQE [10] and NIQMC [11] are used to measure the enhanced performance of different methods. NIQE is the natural image quality evaluator based on statistical regularities from natural and undistorted images. A lower NIQE value denotes a higher image quality. NIQMC is the no-reference image quality metric for contrast distortion, which measures local details and global histogram of the given image to assesses image quality,

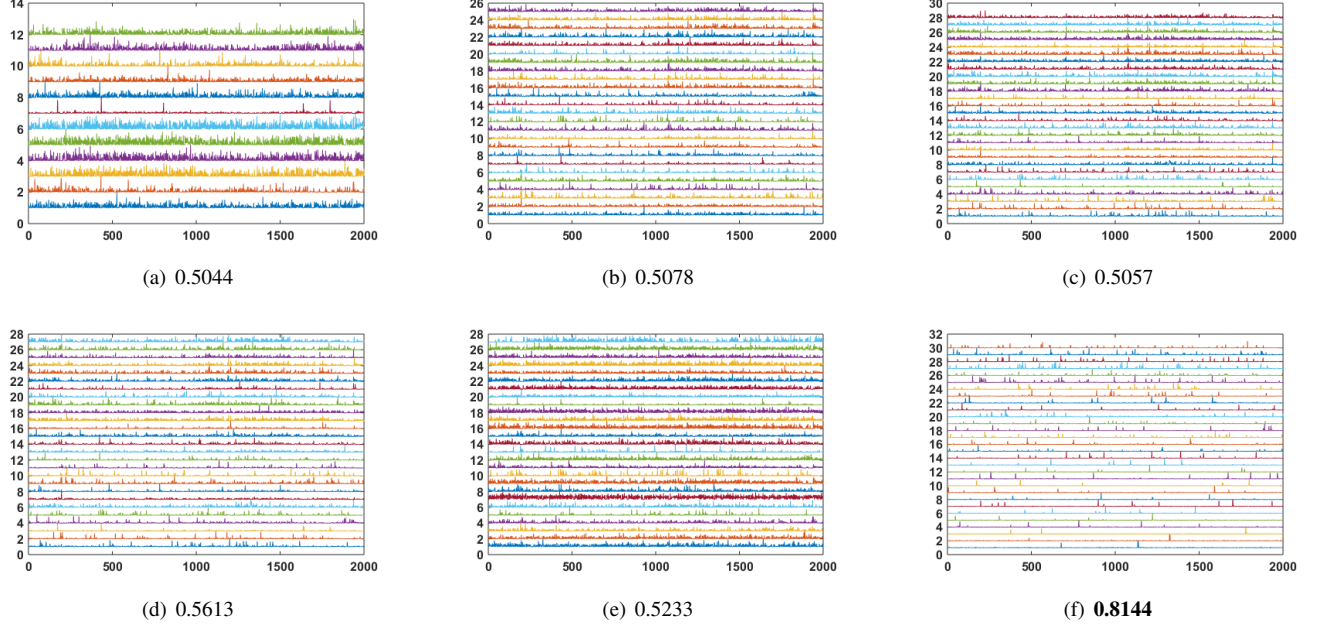


Fig. 1: Temporal activities of all extracted neurons shown in Fig. 11 of our manuscript. The horizontal axis is the video frame number, while the vertical axis is the extracted neuronal number. (a) CNMF [4]. (b) DCP-CNMF. (c) DehazeNet-CNMF. (d) STNeuroNet [5]. (e) DCNMF [6]. (f) DER. Sparseness metrics [3](\uparrow) are shown below, and best results are marked bold.

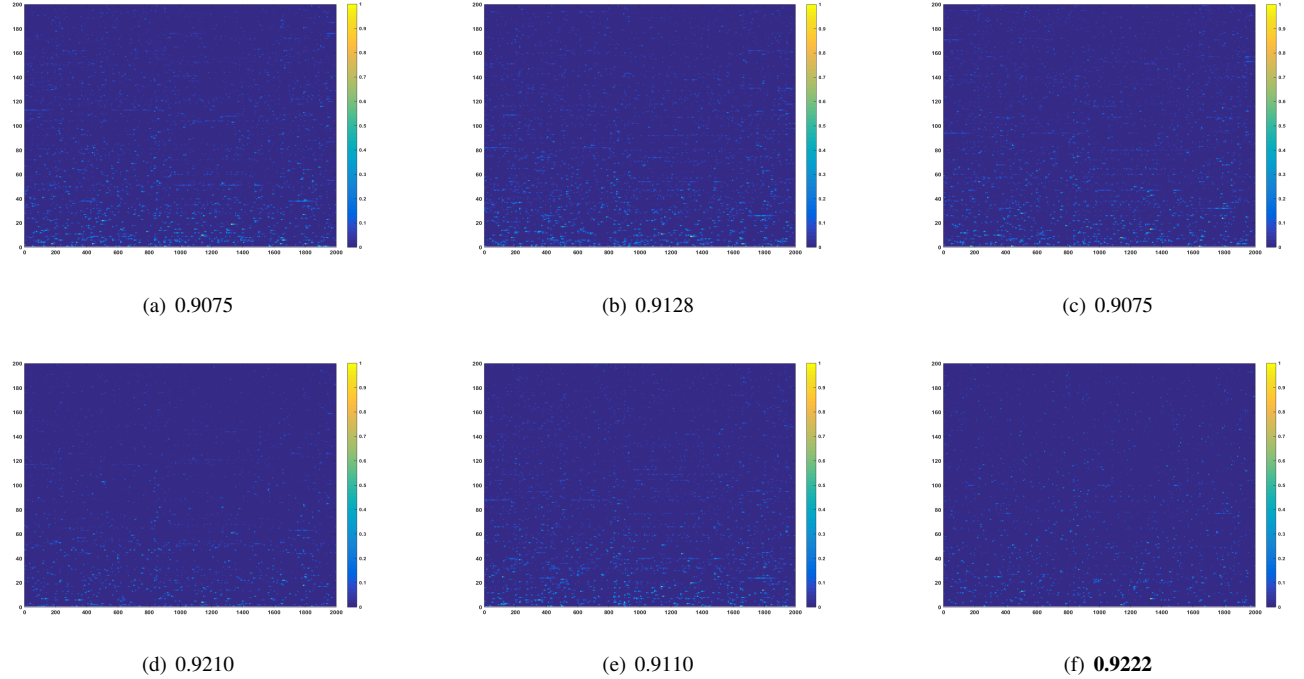


Fig. 2: Temporal activities of all extracted neurons exhibited in Fig. 12 of our manuscript. The horizontal axis is the video frame number, while the vertical axis is the extracted neuronal number. (a) CNMFE [7]. (b) DCP-CNMFE. (c) DehazeNet-CNMFE. (d) STNeuroNet [5]. (e) DCNMFE [6]. (f) DER. Sparseness metrics [3] (\uparrow) are shown below, and best results are marked bold.

and favors images with higher contrast. A larger NIQMC value represents better quality of image contrast.

We apply the proposed depth-dependent transmission model Eq. (15) to estimate the atmospheric light of each pixel for non-uniform illumination removal, and the dichromatic atmospheric light scattering model [1] is reversed to en-

hance non-uniform illumination images of different tissues and organs. The enhanced visual results and corresponding objective metrics (NIQE [10] \downarrow | NIQMC [11] \uparrow) by different methods are shown in Fig. 4. Compared with two methods BPDHE [12] and PIE [13] designed specifically for non-uniform illumination enhancement, our method is superior in

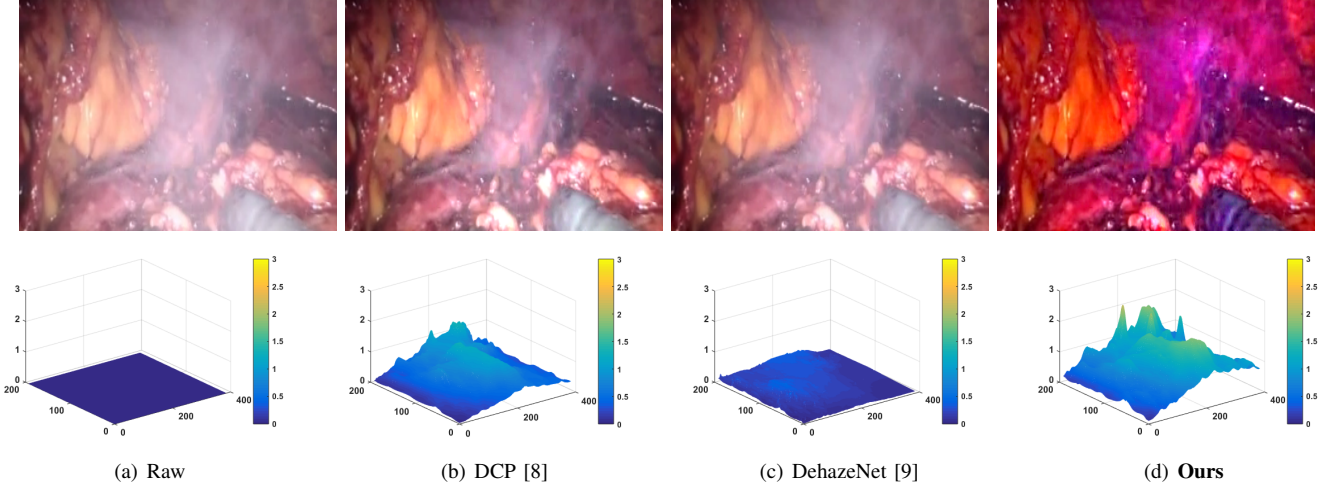


Fig. 3: **Surgical image descattering.** The top row shows descattering results by different methods, and the bottom row shows corresponding depth estimation results. Compared with DCP [8] and DehazeNet [9], our method achieves better descattering results (top row), and our BDCP-based depth estimation model is adopted to produce more accurate depth estimation results (bottom row).

both structure reinforcement and contrast enhancement, and yields better NIQE and NFERM results. This test confirms the validity of our depth-estimation model in non-uniform illumination removal.

REFERENCES

- [1] S. G. NarasimhanShree, S. K. Nayar, "Contrast restoration of weather degraded images," *IEEE Transactions on Pattern Analysis and Machine Intelligence*, vol. 25, no. 6, pp. 713-724, Jun. 2003.
- [2] K. He, J. Sun, X. Tang, "Guided image filtering," *IEEE Transactions on Pattern Analysis and Machine Intelligence*, vol. 35, no. 6, pp. 1397-1409, Jun. 2013.
- [3] P. O. Hoyer, "Non-negative matrix factorization with sparseness constraints," *The Journal of Machine Learning Research*, vol. 5, pp. 1457-1469, Nov. 2004.
- [4] E. A. Pnevmatikakis, D. Soudry, Y. Gao, T. A. Machado, J. Merel, D. Pfau, T. Reardon, Y. Mu, C. Lacefield, W. Yang, M. Ahrens, R. Bruno, T. M. Jessell, D. S. Peterka, R. Yuste, L. Paninski, "Simultaneous denoising, deconvolution, and demixing of calcium imaging data," *Neuron*, vol. 89, no. 2, pp. 285-299, Jan. 2016.
- [5] S. Soltanian-Zadeh, K. Sahingur, S. Blau, Y. Gong, S. Farsiu, "Fast and robust active neuron segmentation in two-photon calcium imaging using spatiotemporal deep learning," *Proceedings of the National Academy of Sciences (PNAS)*, vol. 116, no. 17, pp. 8554-8563, Mar. 2019.
- [6] P. Zhuang, J. Wu, "Reinforcing neuron extraction from calcium imaging data via depth-estimation constrained nonnegative matrix factorization," *IEEE International Conference on Image Processing (ICIP)*, Oct. 2022, pp. 216-220.
- [7] P. Zhou, S. L. Resendez, J. Rodriguez-Romaguera, J. C. Jimenez, S. Q. Neufeld, A. Giovannucci, J. Friedrich, E. A. Pnevmatikakis, G. D. Stuber, R. Hen, M. A. Kheirbek, B. L. Sabatini, R. E. Kass, L. Paninski, "Efficient and accurate extraction of in vivo calcium signals from microendoscopic video data," *eLife*, vol. 7, pp. e28728, Feb. 2018.
- [8] K. He, J. Sun, X. Tang, "Single image haze removal using dark channel prior," *IEEE Transactions on Pattern Analysis and Machine Intelligence*, vol. 33, no. 12, pp. 2341-2353, Dec. 2011.
- [9] B. Cai, X. Xu, K. Jia, C. Qing, D. Tao, "DehazeNet: An end-to-end system for single image haze removal," *IEEE Transactions on Image Processing*, vol. 25, no. 11, pp. 5187-5198, Nov. 2016.
- [10] A. Mittal, R. Soundararajan, A. C. Bovik, "Making a 'completely blind' image quality analyzer," *IEEE Signal Processing Letters*, vol. 20, no. 3, pp. 209-212, Mar. 2013.
- [11] K. Gu, W. Lin, G. Zhai, X. Yang, W. Zhang, C. W. Chen, "No-reference quality metric of contrast-distorted images based on information maximization," *IEEE Transactions on Cybernetics*, vol. 47, no. 12, pp. 4559-4565, Dec. 2017.
- [12] H. Ibrahim, N. S. P. Kong, "Brightness preserving dynamic histogram equalization for image contrast enhancement," *IEEE Transactions on Consumer Electronics*, vol. 53, no. 4, pp. 1752-1758, Nov. 2007.
- [13] X. Fu, Y. Liao, D. Zeng, Y. Huang, X. P. Zhang, X. Ding, "A probabilistic method for image enhancement with simultaneous illumination and reflectance estimation," *IEEE Transactions on Image Processing*, vol. 24, no. 12, pp. 4965-4977, Dec. 2015.